Assessment of Nanomechanical and Tribological Performance of Refractory Nitride-Reinforced Titanium Alloy Matrix Composites Developed by Spark Plasma Sintering

JOHN O. ABE [iD],[1,2,3] OLAWALE M. POPOOLA,[2]
and ABIMBOLA P.I. POPOOLA[1]

1.—Department of Chemical, Metallurgical and Materials Engineering, Tshwane University of Technology, P.M.B. X680, Pretoria, South Africa. 2.—Centre for Energy and Electric Power, Tshwane University of Technology, Pretoria, South Africa. 3.—e-mail: johnabe.fm@gmail.com

The dual-phase titanium alloy Ti6Al4V, presents overall top performance for most-used weight reduction titanium alloy usage in aerospace production, but its general applications have not been fully realized because its resistance to local plastic deformation, friction and wear are unsatisfactory. In a bid to enhance the known shortcomings, Ti6Al4V matrix composites (TMCs) with advanced refractory nitride reinforcements were synthesized by spark plasma sintering. The effects of single (3 wt.%) and double (1.5 wt.% each) reinforcements of nanograde hexagonal boron nitride (h-BN), titanium nitride (TiN) and aluminium nitride (AlN) on the microstructure, phase constituents, nanomechanical and tribological performance of the sintered TMCs were investigated. Microstructure and phase analyses showed that sintered TMCs consist of crack-free microstructures with practically no notable visible defects or impairing intermetallic phases, suggesting that no adverse particle–matrix interfacial reactions occurred during sintering. Nanoindentation and tribology tests generally revealed remarkable improvements in hardness, elastic modulus and wear resistance through each reinforcement type on the sintered TMCs in decreasing order of influence from 3 wt.% h-BN, to 1.5 wt.% of h-BN and AlN, followed by 1.5 wt.% of h-BN and TiN, then 1.5 wt.% of TiN and AlN, to 3 wt.% AlN and finally, 3 wt.% TiN.

INTRODUCTION

Spark plasma sintering (SPS) is one of the most recent, high-tech and innovative non-conventional sintering methods, uniquely different from other powder metallurgy methods primarily by its heating mechanism. SPS employs heating largely by electric spark discharge (spark plasma) generated by low-voltage and large-pulse direct current (Joule heating) plus a uniaxial pressure, which enables the implementation of reduced sintering times because of fast heating/cooling rates and small holding time at sintering temperature, thereby suppressing possible microstructural coarsening.[1,2] Thus, in contrast to the conventional PM technology SPS has been considered a true nonequilibrium processing technique. Moreover, the ability to achieve quick and efficient densification with slight grain growth, improved microstructure and mechanical properties of a large variety of materials—ceramic, polymeric, metallic-based and many more materials—has enabled SPS to take advantage of grain boundary strengthening.[3,4] Hence, the development of nanocomposite materials exhibiting better densification, excellent mechanical attributes like high strength, high hardness etc., with fewer defects is achievable by SPS technology.[5]

Refractory nitrides are a set of technologically important ceramics defined by excellent combination of properties: specific property such as strength (structural applications), high hardness and chemical resistance (wear and corrosion applications),

high-temperature stability and oxidation resistance (high-temperature applications) and high thermal conductivity and electrical insulation (semiconductor applications). Thus, refractory nitrides have been applied in aerospace, automobile, surface, high-temperature technology, electrotechnology, electronics, chemical and metallurgical engineering industries.[6] These refractory nitrides include the nitrides of Al, Si, Ti, B, V, Nb, Ta, Zr and Hf.[7] Literature has reported successful fabrication and impressive characteristics of metal matrix composites (MMCs) with refractory nitride reinforcements. For example, the effect of varying additions of reinforcements (3%, 6% and 9%) on the hardness characteristics of hexagonal boron nitride (h-BN) reinforced aluminium metal matrix composite fabricated by stir casting technique was investigated by Khatavkar et al.[8] Results revealed that hardness improved with increased additions of reinforcements. The microstructure and wear behaviour of titanium nitride-reinforced aluminium-based composites made by powder metallurgy techniques was studied by Mahesh et al.[9] It was revealed that the wear rate of developed composites increased with increased load while an improvement in the wear rate was observed with increasing reinforcement additions from 5 wt.% to 15 wt.% in a step of 5 wt.%. Similarly, the effects of reinforcement particles consisting of 3 wt.% and 6 wt.% BN on the microstructural variation, hardness and oxidation resistance of commercially pure titanium (Cp-Ti) developed by additive manufacturing process were investigated by Avila and Bandyopadhyay.[10] The authors observed secondary phases like TiN and TiB and reported an increase in the hardness of the h-BN-reinforced Cp-Ti composites with increased reinforcement content from 3 to 6 wt%. De Araugo et al.[11] also prepared Al matrix composites through powder metallurgy practice with aluminium nitride (AlN) and silicon nitride (Si_3N_4) reinforcements. The greatest results of the Vickers hardness were found to be directly proportional to the mass fraction of the incorporated reinforcements.

Titanium alloys have attracted tremendous interest for more than half a century. These alloys have found applications as materials for aircrafts' structural parts, maritime components, chemical plants and biomedical implants because of their special combination of properties: light weight, high strength, good chemical resistance and biocompatibility.[12] Within the titanium alloy types in prominent use to date, the dual phase ($\alpha + \beta$) Ti6Al4V titanium alloy presents overall top performance for most-used weight reduction for most-used weight reduction alloy, which accounts for more than half of titanium alloy usage in aerospace production. Thus, the alloy has been considered the workhorse of the aerospace industry.[13,14] Nonetheless, general applications of the alloy have not been fully realized because of its low resistance to localized plastic deformation (or low hardness), which often

engenders severe impairment under extreme friction and wear conditions.[15,16] The concept of the design of titanium matrix composites (TMCs) with advanced reinforcements such as refractory nitrides has pioneered a new innovative materials development approach with important superior properties including improved hardness, specific strength, wear resistance, specific stiffness, elevated temperature stability and durability than its pure titanium alloy counterpart. The development of TMCs began in the aerospace industry and has been growing for about 50 years now.[12,16] Several previous studies presented worthy achievements in TMCs reinforced with refractory nitrides.[4,12,17–19] However, the high cost of synthesizing TMCs remains a hurdle to cross to transition appropriately to practical commercial production.[16,20,21]

TMCs can be produced through either continuous (array of filaments or fibres) or discontinuous (particles or chopped fibres) reinforcement types. Unlike the discontinuously reinforced TMCs (DRTMCs), continuously reinforced TMCs (CRTMCs) come with directional dependence, which makes them vulnerable through the vertical direction and carry the limitation of complex designs and challenge of additional coating cost. On the other hand, discontinuously or particulate reinforced TMCs exhibit relatively lower mechanical properties but are of keen interest because of their lower cost, ease of fabrication, great reproducibility and more isotropic properties, allowing for a large variety of reinforcement types.[12,16,22] The combination of exceptional properties of Ti6Al4V and refractory nitrides, in conjunction with the tremendous benefits of spark plasma sintering operation, a state-of-the-art powder metallurgy technology as earlier mentioned, suggests an interesting prospective means of developing DRTMCs with superior properties.

Recently, the nanoindentation experiment has been seen as a crucial non-destructive test procedure for assessing the mechanical properties of materials at low loads, shallow depths and small scales.[23,24] Nanoindentation is considered a better alternative to the conventional macroscale mechanical testing techniques because many tests can be conducted on a small region more quickly and precisely. Mechanical property testing by nanoindentation technique has been effectively applied to diverse materials such as polymers, ceramics, alloys, compounds and composites, without damaging the microstructural integrity of the materials and removing the need for bulk materials and standard geometries as normally required in conventional mechanical testing. Besides, it enables load–displacement data to be generated for the derivation of a variety of mechanical properties, especially hardness and elastic modulus. Thus, nanoindentation is the most versatile and powerful technique for assessing mechanical properties at the nanoscale.[25,26] The primary objective of this work

was to assess the nanomechanical and tribological performance of refractory nitride-reinforced titanium alloy matrix composites developed by spark plasma sintering of Ti6Al4V alloy matrix and different additions of hexagonal boron nitride (h-BN), titanium nitride (TiN) and aluminium nitride (AlN) nanoparticles with specific focus on single (3 wt.%) and double (1.5 wt.% each) reinforcements as the particulate constituents.

EXPERIMENTAL PROCEDURE

Materials Preparation

The starting materials in this study comprise the commercially pure titanium alloy (Ti6Al4V ASTM Gd5; 60 μm APS and > 99% purity supplied by TLS-Technik GmbH and Co, Germany) as the matrix material and nano-powders of h-BN, TiN and AlN (100 nm APS and > 99% purity supplied by Hongwu International Group Ltd., China) as the reinforcing materials. Six sets of Ti6Al4V matrix powders of the same weight measurement containing varying weight percent (wt.%) of different reinforcements were measured in compliance with the stoichiometric proportion: Ti6Al4V-3 h-BN, Ti6Al4V-3TiN, Ti6Al4V-3AlN, Ti6Al4V-1.5 h-BN-1.5TiN, Ti6Al4V-1.5 h-BN-1.5AlN, Ti6Al4V-1.5TiN-1.5 AlN and a control of pure Ti6Al4V, with a weighing balance (Model EX10202, Canada) of high precision accuracy of 0.001 g. The weighed powders were mixed in a TURBULA shaker mixer (Willy A. Bachofen CH-4132 Type T2F, Switzerland) rotating at a speed of 100 rpm for 10 h to achieve standardized mixtures. While mixing, a couple of small steel balls ($\sim$ 8 mm diameter) were integrated into the powder containers at 2:5 (ball to powder) to impose a certain degree of deformation on the inter-mixed powders and enhance uniformity.[14,27]

Spark Plasma Sintering Process

The illustration of the spark plasma sintering process of the experimental samples is shown in Fig. 1. The required quantity of the prepared powders to produce samples of the TMCs and control of Ø 30 mm by 10 mm dimensions was calculated, measured and poured in the graphite punch-die assembly. The loaded punch-die assembly was secured in the sintering chamber of the spark plasma sintering system (8604 HHPD 25, SPS FCT Systeme GmbH, Germany), and sintering was performed under a vacuum atmosphere of about 4 Pa with constant process parameters: temperature of 1000°C, pressure of 30 MPa, heating rate of 100°C/min and dwell time of 10 min, in line with a Taguchi design and optimization experiment done previously.[19] During sintering, the upper and lower punches transmitted applied pressure and pulsed direct current to the powders, thereby combining both processes of compaction and consolidation in a unit operation. Meanwhile, the temperature of the samples undergoing

sintering was checked intermittently by using an infrared pyrometer located 3 mm directly above the surface of the sample. Later, the pressure of the furnace was released, and the temperature level was reduced to room temperature to end sintering. Subsequently, sandblasting of the as-sintered samples was conducted to eliminate unnecessary graphite remnant sticking to the samples in preparation for testing and characterization.

Microstructure and Phase Characterization

For microstructure characterization, metallographic samples were sliced into cuboid shape (10 mm $\times$ 10 mm $\times$ 5 mm) by wire-cutting and afterward resin-mounted. The samples were ground with "P" grade grit papers ranging from 120 to 4000 and polishing was performed with suspension containing DiaMaxx powder of particle sizes 9 μm, 6 μm, 3 μm and 1 μm to attain a mirror-like polish. Etching of the polished samples was accomplished with Kroll's reagent (2 ml hydrofluoric acid; 5 ml nitric acid and 100 ml water). The metallographic examination of the etched samples was conducted by using a scanning electron microscope (TESCAN VEGA3, Czech Republic) combined with an energy-dispersive spectroscope (SEM/EDS) operated at 20-kV acceleration voltage and an optical microscope (Olympus BX 51 TRF, Japan), respectively. For phase characterization, the x-ray diffraction (XRD) patterns of the samples were recorded by using Philips PW1710 x-ray diffractometer model with CuKα radiation (1.54060 Å wavelength) and the diffraction angles (2θ) were collected between 10° and 90° (40 kV acceleration voltage) performed in step mode (0.02° size). The phase identification was performed with the aid of PANalytical X'Pert Highscore Plus in conjunction with OriginPro 2019b software package. Subsequently, the individual contributions of crystallite sizes and lattice strains on the true peak broadening in the XRD diffractograms of the sintered samples were estimated by using Williamson-Hall (W–H) plot method. Gaussian function was effectively employed to fit the broadening of the XRD peaks, and averages of seven most intensive diffraction peaks were selected to calculate the crystallite size and lattice strain. The average crystallite size, L, of the samples is calculated from the full width at half maximum (FWHM), $\beta_{\text{crystalline}}$, which is the peak broadening due to small crystallite sizes measured on the diffraction profile values by using Scherrer's formula given in Eq. 1.[28]

$$\text{Crystallite size}, L = \frac{K\lambda}{\beta_{\text{crystalline}} \cos\theta} \qquad (1)$$

where K is termed the Scherrer constant (taken to be 0.94), λ is the CuKα radiation wavelength (0.154060 nm), and θ is the peak diffraction angle. By rearranging Eq. 1, we get:
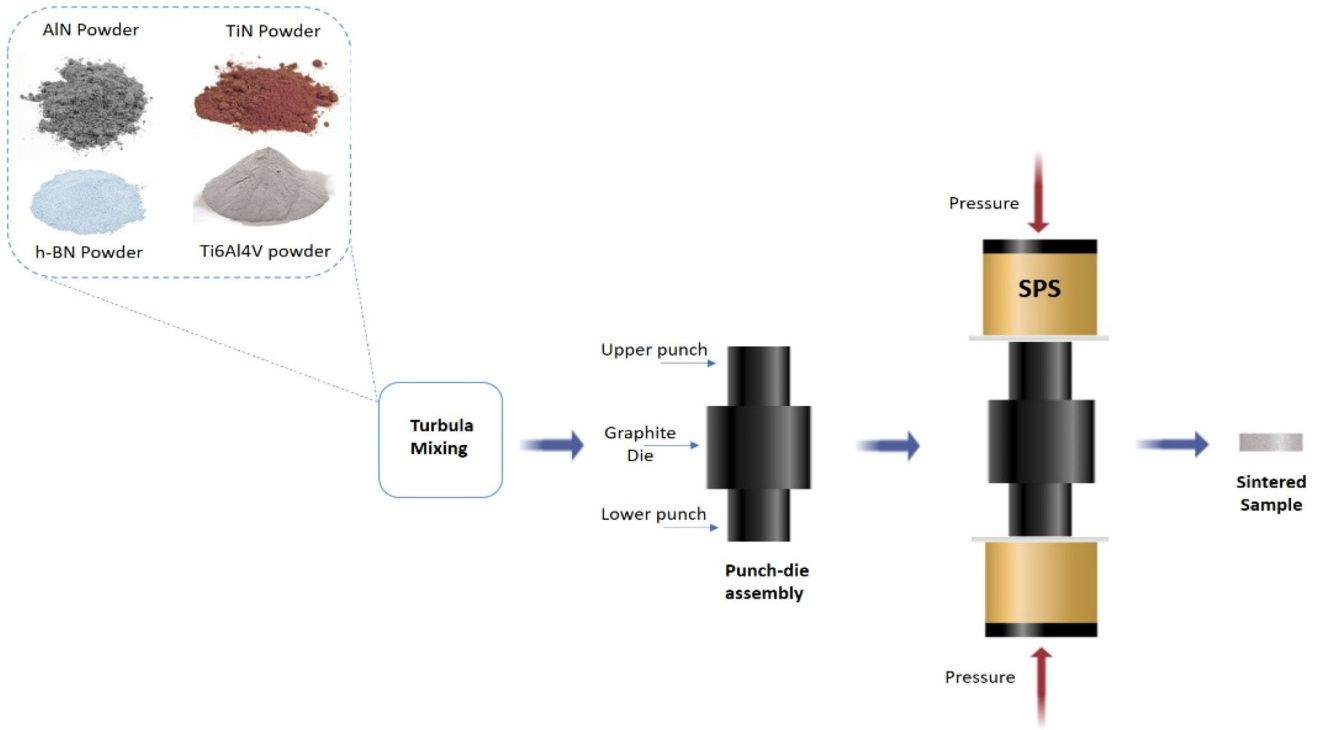
Fig. 1. Illustration of the spark plasma sintering process.

$$\beta_{\text{crystalline}} = \frac{K\lambda}{L\cos\theta} \tag{2}$$

On the other hand, the average lattice strain, ε, of the samples is calculated from the XRD data by using Wilson's formula given in Eq. 3.[29]

$$\text{Lattice strain}, \varepsilon = \frac{\beta_{\text{strain}}}{4\tan\theta} \tag{3}$$

where β_{strain} is the peak broadening due to the lattice strain and θ is the peak diffraction angle. By rearranging Eq. 3, we get:

$$\beta_{\text{strain}} = 4\varepsilon\tan\theta \tag{4}$$

According to the W–H method, assuming that the crystallite size and the lattice strain contributions to the peak broadening in the XRD diffractograms are independent of each other, the true broadening, β_{hkl}, is given by the sum of Eqs. 2 and 4 as follows:

$$\beta_{hkl} = \beta_{\text{crystalline}} + \beta_{\text{strain}} = \frac{K\lambda}{L\cos\theta} + 4\varepsilon\tan\theta \tag{5}$$

By rearranging Eq. 3, we get:

$$\beta_{hkl}\cos\theta = 4\varepsilon\sin\theta + \frac{K\lambda}{L} \tag{6}$$

Equation 6 represents a straight-line graph equation, where $\beta_{hkl}\cos\theta$ is plotted against $4\varepsilon\sin\theta$ and ε is the slope of the line while $\frac{K\lambda}{L}$ is the y-intercept. In the study, W–H graphs for the sintered samples were plotted and a linear fit of the scattered results

were taken. From the linear fit, L was estimated by comparing the y-intercept with $\frac{K\lambda}{L}$ in Eq. 6, and ε was estimated from the slope of the fit, respectively.[28,29]

Nanoindentation Test

The nanomechanical performance of the TMCs was assessed in accordance with ISO 14577 by using an Anton Paar Nanoindenter (NHT) set up with a Berkovich indenter. The nanoindentation test was performed at a constant applied load of 200 mN, penetration, holding and retracting time of 20 s. An average of six to ten indentation measurements at different points selected on the sample's surface were taken and recorded for each sample. The nanoindentation technique was based on Oliver-Pharr analysis, where hardness, H (in MPa), and elastic modulus, E (in GPa), of the samples were evaluated using Eqs. 7 and 8.[25,30]

$$H = \frac{P\text{max}}{Ac} \tag{7}$$

where Ac is the projected contact area between the sample and the indenter at the maximum load $P_{\max}$

$$\frac{1}{Er} = \frac{1 - Vs^2}{Es} + \frac{1 - Vi^2}{Ei} \tag{8}$$

where E_i and E_s are the elastic moduli of the indenter and sample, respectively; E_r is the reduced elastic modulus, which has taken into consideration

Assessment of Nanomechanical and Tribological Performance of Refractory Nitride-Reinforced
Titanium Alloy Matrix Composites Developed by Spark Plasma Sintering

795

the individual contributions of E_i and E_s, whereas v_i and v_s are the Poisson's ratio of the indenter and the sample, respectively.

Tribology Test

Tribological properties of materials deal with the different friction, wear and lubrication behaviour tendencies of these materials when they are in relative motion or subjected to different operating conditions. The tribology test was performed by using a TRB[3] pin-on-disk tribometer (manufactured by Anton Paar Tritec SA, Switzerland) at room temperature with a rotary wear module. A Ø 10 mm steel ball was used as a counter body of roller against the samples. Three normal loads of 5 N, 10 N and 15 N were applied at a speed rotating at 150 rpm. The patterns of fluctuations of the coefficient of friction (COF), the average COF values and the specific wear rates were observed for all the samples throughout the test.

RESULTS AND DISCUSSION

SEM and Phase Analyses of the Starting Materials

The SEM and XRD characterizations of the powders and sintered materials are key procedures performed for adequate understanding of the preliminary structures of the materials, the evolution of various phases, sintering process reactions and the mechanisms responsible for the materials' properties. Figure 2(a–d) portrays the SEM photographs of the powders used generally in this work consisting of Ti6Al4V titanium alloy, h-BN, TiN and AlN. Figure 2a clearly shows spherical particles of Ti6Al4V alloy, Fig. 2b reveals platy-hexagonal particles of h-BN, Fig. 2c presents lumpy spherical particles of TiN while Fig. 2d shows wurtzite-like particles of AlN. Similarly, different patterns obtained from the XRD characterization of the powders are shown in Fig. 2(a-d). The XRD pattern obtained for Ti6Al4V titanium alloy powder in Fig. 3a gives a vivid indication of pristine α phase peaks appearing at the diffraction angle, $2\theta = 35.09°$, $38.42°$, $40.17°$, $53.0°$, $62.95°$, $70.66°$, $76.22°$ and $77.37°$ equivalent to (100), (002), (101), (102), (110), (103), (112) and (201) planes, respectively, where there was no evidence of other peaks conforming to any other phase. Figure 3b shows a very high-intensity peaks of crystalline hexagonal BN phase only occurring at $2\theta = 26.63°$, $41.51°$, $43.75°$, $50.0°$, $54.85°$, $75.73°$ and $81.93°$ matching (002), (100), (101), (102), (004), (110) and (105) planes, representing an average particle size of 100 nm produced via isothermal annealing. Similarly, crystalline TiN phase can be identified in Fig. 3c at $2\theta = 36.66°$, $42.6°$, $61.81°$, $74.07°$ and $77.96°$ equivalent to (111), (200), (220), (311) and (222) planes while clear peaks of crystalline AlN phase can be seen in Fig. 3d occurring at $2\theta = 33.22°$, $36.04°$, $37.92°$, $49.82°$,

59.35°, 66.05°, 69.73°, 71.44°, 72.63°, 76.45° and 81.1° matching (100), (002), (101), (102), (110), (103), (200), (112), (201), (004) and (202) planes.

SEM/EDS and Phase Analyses of the Sintered TMCs

Figure 4(a–g) presents typical SEM and respective EDS photographs revealing the microstructural formation and intensity peaks of Ti6Al4V alloy, Ti6Al4V-3 h-BN, Ti6Al4V-3TiN, Ti6Al4V-3AlN, Ti6Al4V-1.5 h-BN-1.5TiN, Ti6Al4V-1.5 h-BN-1.5AlN and Ti6Al4V-1.5TiN-1.5 AlN sintered at 1000°C temperature, 30 MPa pressure, 100°C/min heating rate and 10-min dwelling time, respectively. A representative microstructure of the spark plasma-sintered Ti6Al4V alloy is shown in Fig. 4a with primarily two distinct phases comprising α and β stabilized by the aluminium and vanadium contents in the titanium alloy, respectively, as supported by the EDS spectra presenting the elemental peaks of the plausible amounts. The primary lamellar colonies of α phase can be observed having different orientations as well, which is typical of a α/β titanium alloy.[31,32] On the other hand, based on Fig. 4(b–g), obvious transformations are occurring within the α/β alloy matrix. Different morphological developments in the specific microstructure of each TMC could be linked to the effect of different additions of the refractory nitride reinforcement types. The respective EDS spectra as can be seen in Fig. 4(a–g), showing the elemental peaks of expected compositions as a fair confirmation of the inclusion of the nitride reinforcement particles in the α/β matrix for all the TMCs.[33] Figure 4b gives a noticeable picture of h-BN particles uniformly distributed in the α/β alloy matrix, a desirable attribute for better material properties. The microstructures taken for the other two single reinforcement types can be seen in Fig. 4c and d for TiN and AlN, respectively, in the sintered TMCs. There was a microstructural transformation from the predominant lamellar colonies of α-Ti alloy matrix to a bimodal structure largely consisting of a distribution of $\alpha + \beta$ structures upon the addition of 3 wt.% TiN reinforcement in Fig. 4c while Fig. 4d displays a SEM photograph of coarsened AlN mainly since the particulate reinforcement tended to agglomerate, but was quite homogeneously distributed in the α/β alloy matrix. Figure 4(e–g) presents the SEM images taken for double reinforcement type category of the sintered TMCs. Distinct intermixture of double reinforcements in α/β microstructure displaying thicker and longer coarsened lamellar α phase in a β-matrix can be observed in each photograph. For instance, Fig. 4e reveals patterns of h-BN and TiN particles propagated along the grain boundaries. Meanwhile, a homogeneous intermixture of both reinforcements of h-BN and AlN particle embedment can be seen in Fig. 4f, and nearly the same pattern formation (as
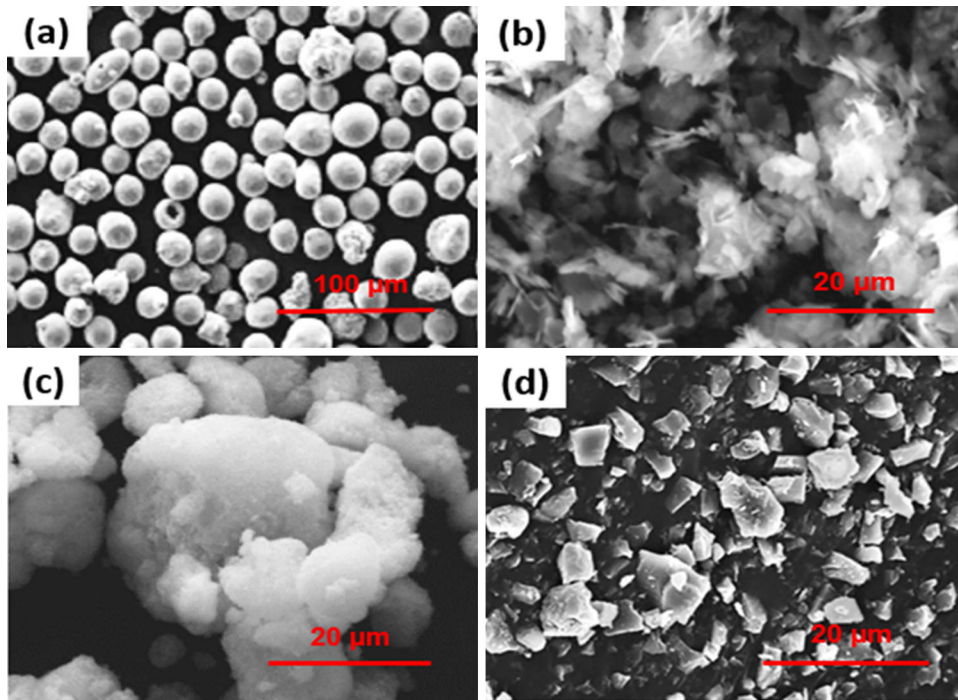
Fig. 2. Typical SEM photographs of as-received powders: (a) Ti6Al4V (b) *h*-BN (c) TiN (d) AlN.
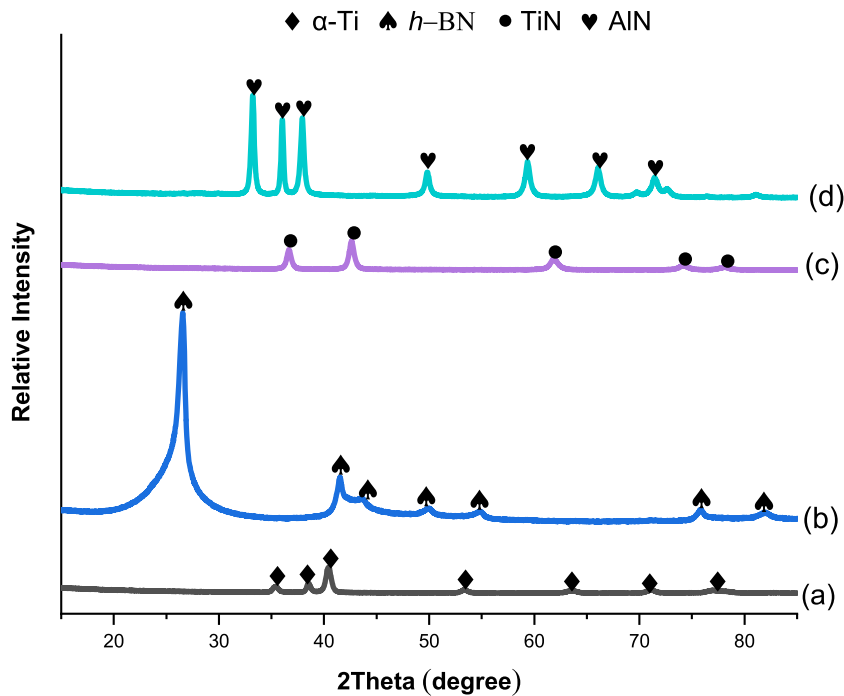

Fig. 3. Typical XRD patterns of as-received powders: (a) Ti6Al4V (b) *h*-BN (c) TiN (d) AlN.

in Fig. 4f) is shown in Fig. 4g but with an appearance of dendrite-like structure comprising basically TiN and AlN particles.[33,34] The SEM results revealed that the sintered compacts are made up of crack-free microstructures with practically no notable visible porosities or other major defects that may be detrimental to their ensuing properties.

The plots of the XRD characterization performed on the spark plasma-sintered samples have been stacked as shown in Fig. 5(a–g). For the sintered Ti6Al4V titanium alloy in Fig. 5a, the XRD diffractogram shows that only the α and β phases are present.[12,39] Close observation of other XRD plots is shown in Fig. 5(b–g); diffraction peaks of α phase
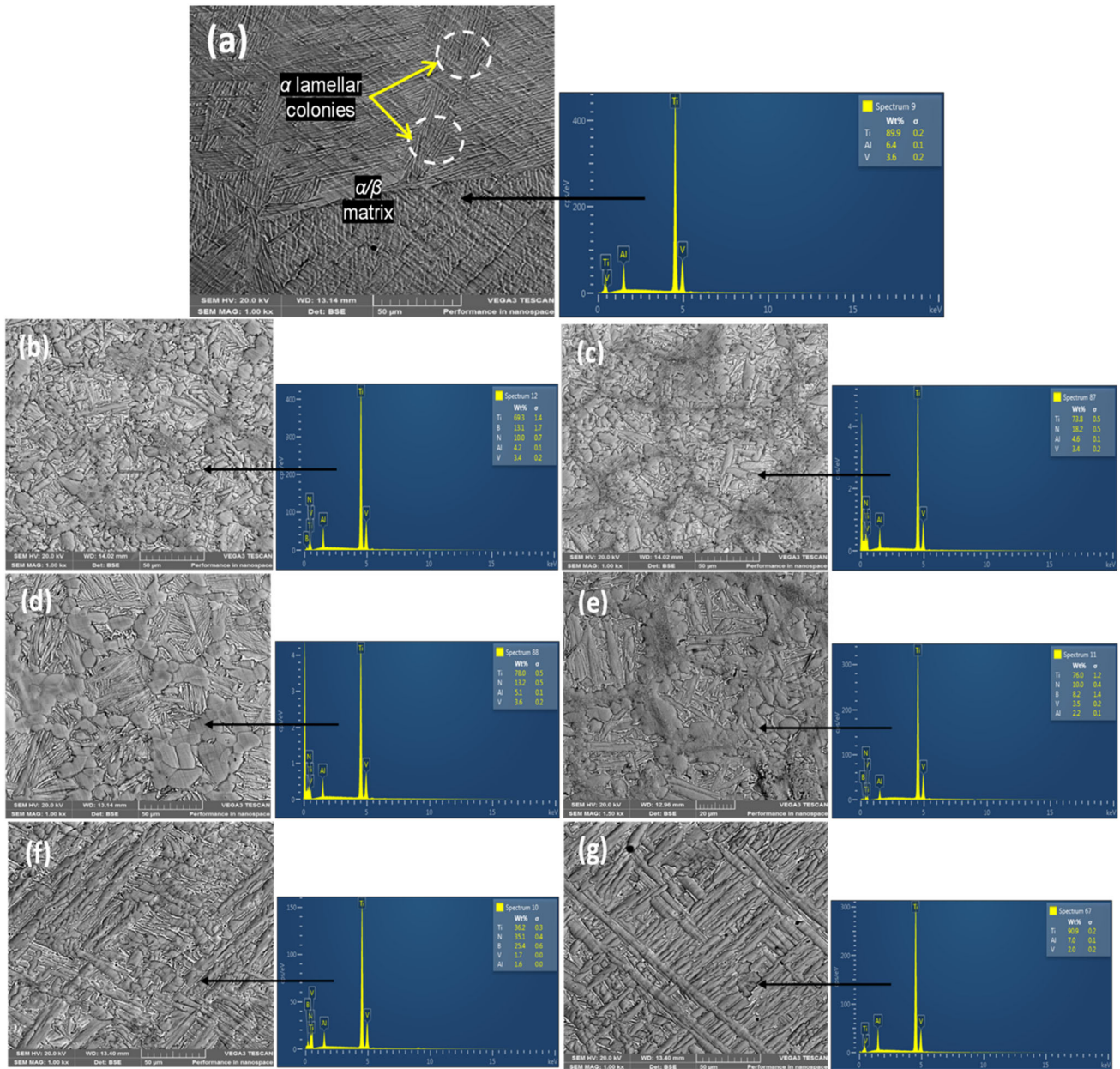
Fig. 4. Typical SEM and EDS photographs displaying the morphologies and elemental peaks of as-sintered materials: (a) Ti6Al4V alloy (b) Ti6Al4V-3 h-BN (c) Ti6Al4V-3TiN (d) Ti6Al4V-3AlN (e) Ti6Al4V-1.5 h-BN-1.5TiN (f) Ti6Al4V-1.5 h-BN-1.5AlN (g) Ti6Al4V-1.5TiN-1.5AlN.

also appeared at certain positions including 2θ–35°, 40°, 53°, 62° and 70° matching (100), (002), (101), (102), (110) and (103) planes, respectively, probably because all the sintered materials benefitted from a mutual matrix. In addition to the peaks of prominent α phases identified already in Fig. 5(b–g), other secondary phases were detected as well. For instance, the XRD pattern of Ti6Al4V-3 h-BN as depicted in Fig. 5b shows the presence of phases of BN occurring at $2\theta \sim 26.8°$ and 41.6°, titanium boride, TiB, at $2\theta \sim 35.3°$ and 38.3°, vanadium nitride, VN, at $2\theta \sim 42.2°$ and $\sim 61.2°$ and AlN at $2\theta \sim 36.0°$. Figure 5c, d and g shows the XRD profiles of Ti6Al4V-3TiN, Ti6Al4V-3AlN and

Ti6Al4V-1.5TiN-1.5AlN, respectively, and that certain secondary phases are present at approximately the same diffraction angles including TiN at 2θ 36.6° and 42.6° and VN at $2\theta \sim 37.6°$ and 43.7°, whereas AlN phase can be seen in Fig. 5g appearing at $2\theta \sim 33.0°$ and 38.0°. Furthermore, characteristic peaks of TiB phase were observed at $2\theta \sim 35.3°$ and 38.3°, TiN phase at $2\theta \sim 36.6°$ and 42.6°, VN phase at $2\theta \sim 37.6°$ and 43.7° and BN phase at $2\theta \sim 43.3°$, respectively, in Fig. 5e, denoting Ti6Al4V-1.5 h-BN-1.5TiN. Meanwhile, the XRD profile in Fig. 5f representing Ti6Al4V-1.5 h-BN-1.5AlN shows the peaks of AlB phase appearing at $2\theta \sim 37.0°$, TiN and BN phases at $2\theta \sim 43.3°$, respectively. From the
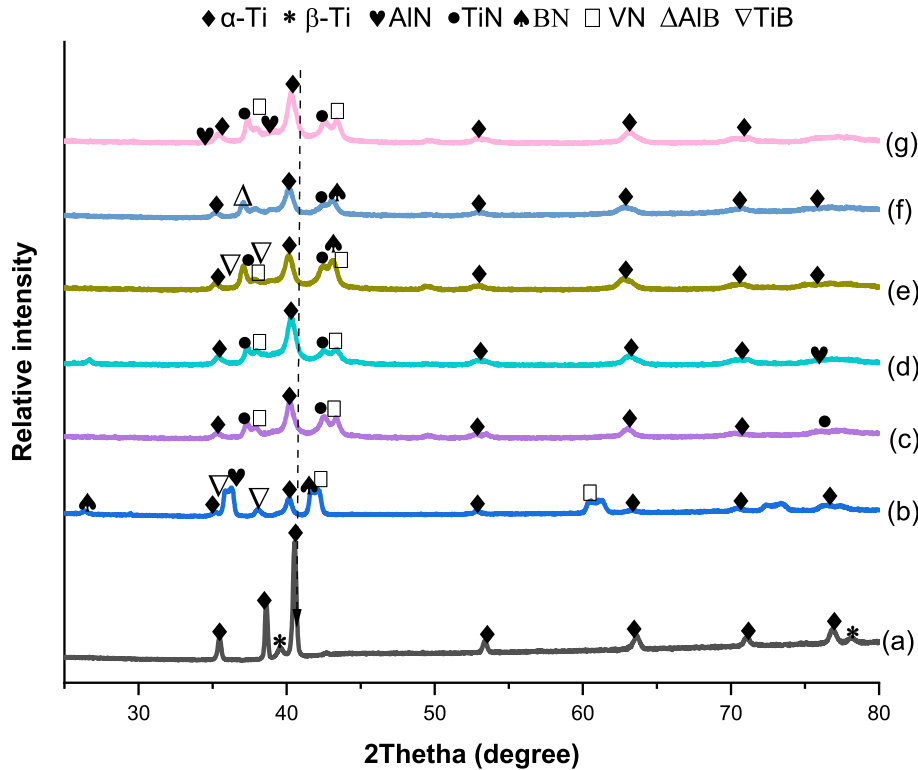
Fig. 5. Typical XRD patterns of sintered materials: (a) Ti6Al4V alloy (b) Ti6Al4V-3 *h*-BN (c) Ti6Al4V-3TiN (d) Ti6Al4V-3AlN (e) Ti6Al4V-1.5 *h*-BN-1.5TiN (f) Ti6Al4V-1.5 *h*-BN-1.5AlN (g) Ti6Al4V-1.5TiN-1.5AlN.

assessment of the XRD results, it is obvious that impairing intermetallic phases that tend to adversely affect material properties were not detected, suggesting that no adverse reactions occurred at the particle–matrix interfaces throughout the sintering operation.

According to the XRD profiles of the powder materials shown in Fig. 3(a–d) before sintering and in comparison with the XRD profiles of the sintered materials shown in Fig. 5(a–g), considerable reduction in the original relatively high peak intensities of the Ti6Al4V alloy matrix and the reinforcement nanoparticles comprising *h*-BN, TiN and AlN can be observed, which is closely related to the broadening of the XRD peaks of the sintered TMCs. This could mainly be due to decomposition and thorough dispersion of the particulate nano-reinforcements on the Ti6Al4V alloy matrix during the intense TURBULA mixing and sintering processes that caused some microstructural modifications and formation of secondary phases. The broadening of the XRD peaks is indicative of the presence of nano-sized crystals and a function of the crystallite sizes and induced lattice strains in the sintered TMCs.[35] It is equally important to note that the individual effect of average crystallite size, L, and average lattice strain, ε, that resulted in the broadening of the XRD peaks of the sintered samples were estimated by using W–H approach. The W–H plots for the samples were drawn and a linear fit of the scattered results was considered. From the linear

fit, L was estimated by comparing the y-intercept with $\frac{K\lambda}{L}$ as given in Eq. 6, and ε was estimated from the slope of the fit. The results obtained are presented in the graph in Fig. 6.[28,29]

From Fig. 6, the values obtained for the average crystallite size of the sintered TMCs could be observed to decrease in all cases compared to that of the unreinforced titanium alloy with the highest average crystallite size of ∼ 67.35 nm. Thus, the XRD peaks of the TMCs in Fig. 5(b–g) broaden out compared to the sharp XRD peaks of the Ti6Al4V matrix in Fig. 5(a). The apparent refinement and variation in the crystallite sizes of the TMCs could be due to the influence of the nano-sized particles of the refractory nitride reinforcements which also aided fast heating and cooling of the composite samples during the SPS processing. According to Eq. 9 depicting the Hall–Petch equation, as the average crystallite size of the TMCs decreases, the average grain diameter also decreases leading to the increase in hardness and strengthening of the TMCs.[36]

$$\sigma_y = \sigma_o + kd^{-\frac{1}{2}} \tag{9}$$

where σ_y stands for the yield stress, σ_o stands for the original yield stress required to initiate plastic flow at a grain boundary, k stands for the material's constant, and d stands for the average grain diameter. Similarly, the slopes of the W–H plots obtained are positive suggesting that tensile strains

Assessment of Nanomechanical and Tribological Performance of Refractory Nitride-Reinforced Titanium Alloy Matrix Composites Developed by Spark Plasma Sintering
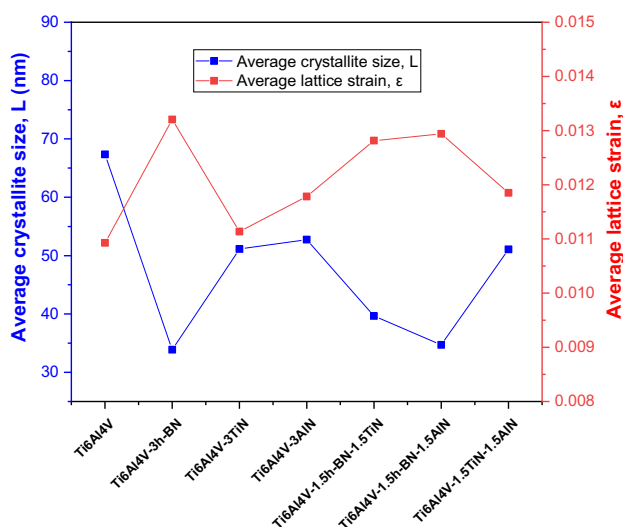
799

Fig. 6. Comparison between the estimated average crystallite size and induced lattice strain of the sintered titanium alloy matrix and TMCs.

are induced by the inclusion of the refractory nitride nano-reinforcements in the lattice of the sintered TMCs. Broadening of the XRD peaks and a slight shift towards the lower diffraction angles on the left side of the XRD diffractograms in Fig. 5(b–g) were observed.[37,38] The estimated average lattice strain, ε, can be noticed to vary in an inverse manner with most of the average crystallite size of the TMCs. The induction of lattice strain in the TMCs is an indication of structural changes that can enhance the free energy which could bring about improvement in the mechanical properties.[36,38]

Nanomechanical Analysis of the Sintered TMCs

In a bid to assess the nanomechanical performance of the sintered TMCs, the comparison between the nanoindentation load–displacement and penetration depth-time curves derived by using Oliver and Pharr method are presented in Fig. 7a and b, respectively, while the comparison between the nanoindentation hardness values and elastic modulus values are presented in Fig. 7c and d, respectively, for the titanium alloy matrix and sintered TMCs subjected to 200 mN indentation load. From the nanoindentation load–displacement graph in Fig. 7a, a comparable loading and unloading trend that is smooth without any pop-in effects can be observed for all the tested samples, where the load–displacement curves displayed an elastic–plastic deformation behaviour.[40] The region between the loading–unloading curves of Ti6Al4V alloy matrix appears wide with the largest displacement which suggests that the alloy's resistance to plastic deformation is low, which is not unusual because of the ductility of the titanium alloy.[41] Additionally, the alloy matrix displayed the highest penetration depth as shown in Fig. 7b. This implies

that the indenter's tip penetrates the alloy matrix with greater ease compared to the reinforced TMCs. It is recognized that the extent of penetration depth has correlation with hardness of the material. Thus, the least nanoindentation hardness and elastic modulus values of 5838 ± 322.63 MPa and 115.07 ± 3.63 GPa were measured for the alloy matrix (see Fig. 7c and d).[25,40] Furthermore, Fig. 7a shows that the regions between the loading–unloading curves of the reinforced TMCs appear narrow with a major shift towards the left which indicates that the reinforcements effectively minimize the displacements owing to the load sharing of the TMCs.[26,40] Meanwhile, the penetration depth of the reinforced TMCs as shown in Fig. 7b reduced drastically with time and this is true for all reinforcements, although to different extents. Contrary to the unreinforced Ti6Al4V alloy with the maximum penetration depth of 1446.2 nm, the sintered Ti6Al4V-1.5TiN-1.5AlN showed a decline in maximum penetration depth of 1055.3 nm which is the highest among the sintered TMCs, while Ti6Al4V-3 h-BN showed the highest resistance to the indentation load with the least maximum penetration depth of 495.6 nm. This suggests that there is a massive reduction in the initial plastic deformation behaviour of the titanium alloy upon reinforcement and reasonably explains why the slope of the loading and unloading curves of the TMCs increased, where the slope of the unloading part of the curve depicts stiffness which is closely related to the elastic modulus of the materials.[26] The improved nanomechanical properties (hardness, stiffness and elastic modulus) are mainly due to the mechanism of load transfer from the Ti6Al4V alloy matrix to the comparatively harder reinforcement particles which induced dispersion strengthening acting as an effective hindrance to dislocation motion.[40,42]

According to Fig. 7c and d, there is continuing enhancement in nanoindentation hardness values (8731 ± 455.68—$63,908 \pm 758.05$ MPa) and elastic modulus (155.46 ± 5.68—335.05 ± 4.05 GPa) of the TMCs when compared with the unreinforced Ti6Al4V alloy (hardness and elastic modulus values of 5838 ± 322.63 MPa and 115.07 ± 3.63 GPa, respectively). It can further be summarized that the nanoindentation hardness value of Ti6Al4V-3 h-BN ($63,908 \pm 758.05$ MPa) is superior to the unreinforced Ti6Al4V alloy by 995%, about 632% above Ti6Al4V-3TiN (8731 ± 455.68 MPa) and exceeds Ti6Al4V-3AlN ($11,832 \pm 587.54$ MPa) by 440% in the single reinforcements' category, whereas the nanoindentation hardness value of Ti6Al4V-1.5 h-BN-1.5AlN ($60,775 \pm 672.08$ MPa) is approximately 941% superior to the unreinforced Ti6Al4V alloy, about 105% above Ti6Al4V-1.5 h-BN-1.5TiN ($29,653 \pm 559.11$ MPa) and 411% more than Ti6Al4V-1.5TiN-1.5AlN ($11,898 \pm 350.66$ MPa) in the double reinforcements' category as portrayed in Fig. 7c. Zhang et al.[43] mentioned that the
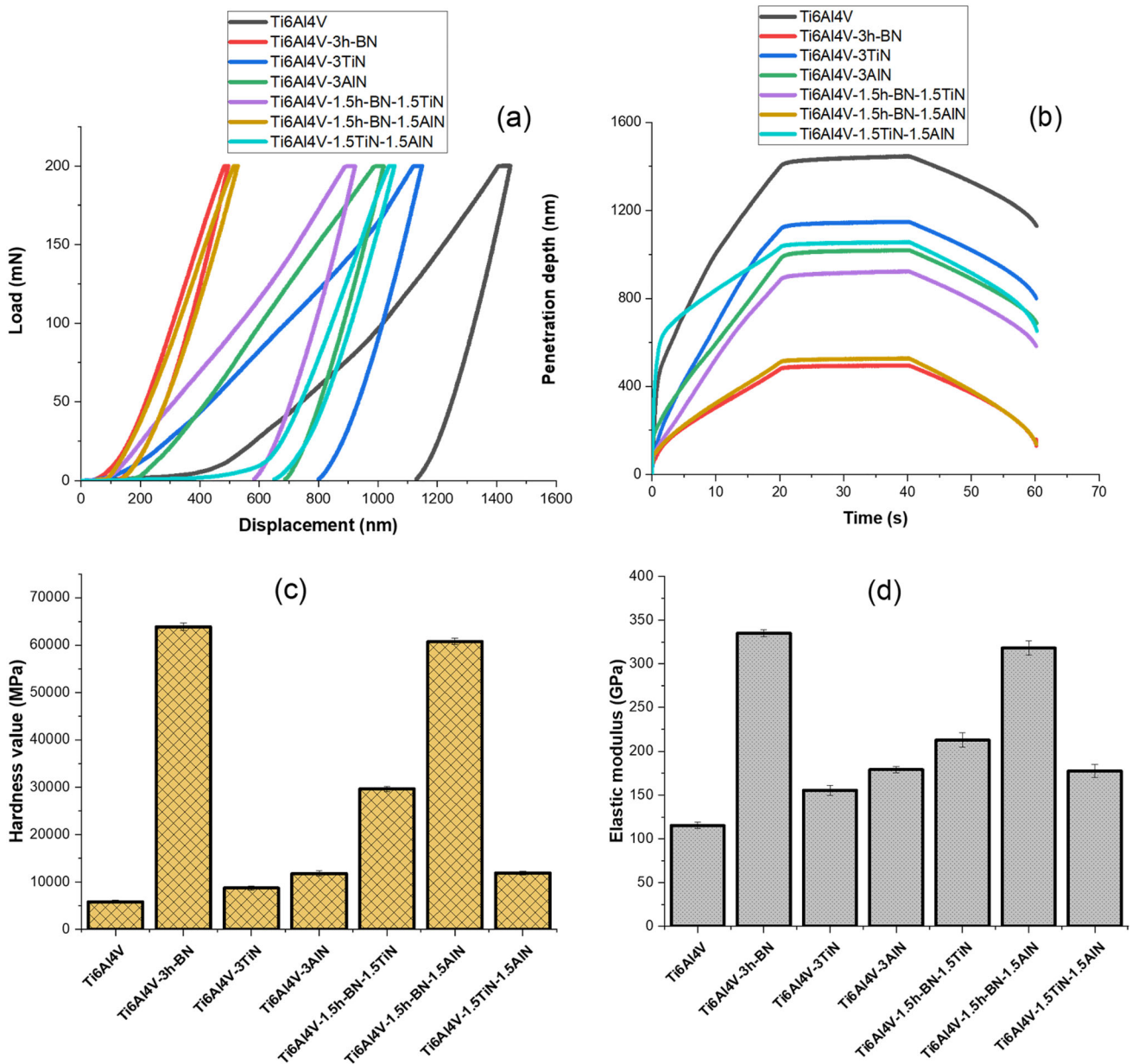
Fig. 7. Comparison between nanoindentation. (a) Load–displacement graphs. (b) Penetration depth-time graphs. (c) Hardness values. (d) Elastic modulus values of the titanium alloy matrix and sintered TMCs.

strength of a material is proportional to its hardness. This implies that a material which possesses higher hardness at the same time possesses higher strength. Since the sintered TMCs in this study have higher hardness than the common Ti6Al4V alloy, the expectation is that the TMCs possess enhanced strength as well.[44] Similarly, the nanoindentation elastic modulus value of Ti6Al4V-3 h-BN (335.05 ± 4.05 GPa) is superior to the unreinforced alloy by 191%, about 116% above Ti6Al4V-3TiN (155.46 ± 5.68 GPa), and exceeds Ti6Al4V-3AlN (179.05 ± 3.54 GPa) by 87% in the single reinforcements' category, while the elastic modulus value of Ti6Al4V-1.5 h-BN-1.5AlN (318.1 ± 8.08 GPa) is approximately 176% superior to the unreinforced

Ti6Al4V alloy, about 79% above Ti6Al4V-1.5TiN-1.5AlN (177.58 ± 7.66 GPa) and 49% greater than Ti6Al4V-1.5 h-BN-1.5TiN (213.02 ± 8.11 GPa) in the double reinforcements' category as presented in Fig. 7d. Consequently, nanoindentation elastic modulus depicted a similar trend in improvement as the nanoindentation hardness values, meaning that these nanomechanical properties are mutually proportional for the tested materials.[44] Moreover, it is important to mention that the nanoindentation test results showed that the different reinforcement additions combined with the effectiveness of the SPS consolidation technique have yielded a meaningful improvement of the nanomechanical performance (hardness and elastic modulus) of the α/β

titanium alloy matrix mainly due to the development of good particle–matrix bonding and mechanism of load transfer from the alloy matrix to the harder reinforcement particles.[25,45]

Tribological Analysis of the Sintered TMCs

Following the assessment of the effects of single and double reinforcement types consisting of h-BN, TiN and AlN nanoparticles on the nanoindentation hardness values of the sintered Ti6Al4V alloy matrix composites, which is known to have an important effect on tribological properties,[46] the changes in the COF and specific wear rates were investigated and discussed in this section. Figure 8 shows the comparison of the variation of COF with sliding time between the Ti6Al4V alloy matrix and the TMC samples comprising of Ti6Al4V-3 h-BN, Ti6Al4V-3TiN, Ti6Al4V-3AlN, Ti6Al4V-1.5 h-BN-1.5TiN, Ti6Al4V-1.5 h-BN-1.5AlN and Ti6Al4V-1.5TiN-1.5 AlN, specifically in the selected applied load of 10 N as a representative change occurring in the COF during the friction process while the average COF of the unreinforced alloy matrix and those of the TMCs as a function of the reinforcement types under the applied loads of 5 N, 10 N and 15 N are compared in Fig. 9. As displayed in Fig. 8, the variation of COF values at the initial stage described as the running-in period are quite distinct with varying magnitudes for all the samples with Ti6Al4V alloy matrix showing the highest magnitude of COF and relatively short running-in period.[47] At the steady-state period, the variation in the COF values observed was reasonably stabilized for all the samples and ranged between 0.02 and 0.48. Figure 9 clearly shows that the average COFs of all the TMC samples are generally lower in contrast to the unreinforced matrix alloy as the applied normal load increased from 5 N toward

15 N. It is obvious (as shown in Fig. 9) that the average COF varied directly from 0.28 ± 0.02 to 0.5 ± 0.035 for the unreinforced alloy, while a similar trend can be observed for all the TMC samples but at relatively lower values. In the binary composite samples category, the average COF values for Ti6Al4V-3 h-BN varied from 0.08 ± 0.011 to 0.24 ± 0.021, Ti6Al4V-3TiN varied from 0.27 ± 0.015 to 0.46 ± 0.048 and Ti6Al4V-3AlN varied from 0.23 ± 0.013 to 0.4 ± 0.03. Meanwhile, for the ternary composite samples, the average COF of Ti6Al4V-1.5 h-BN-1.5TiN varied from 0.18 ± 0.014 to 0.41 ± 0.026, Ti6Al4V-1.5 h-BN-1.5AlN varied from 0.13 ± 0.011 to 0.32 ± 0.019 and Ti6Al4V-1.5TiN-1.5AlN from 0.17 ± 0.02 to 0.38 ± 0.034. By the assessment of the results, it can be found that the highest set of values of average COF were obtained for the unreinforced alloy samples and the lowest set of average COF values were obtained for Ti6Al4V-3 h-BN samples. The extremely low average COF of 0.08 ± 0.011 recorded for Ti6Al4V-3 h-BN under the applied load of 5 N gives an indication of the lubricity of the TMC sample credited to the inclusion of smooth and lubricious h-BN content.[48] It can also be deduced that the COF is generally connected to the fundamental interaction of asperities between the counter bodies which in microscale tended to vary within a specific range during the experimentation. This is also the main reason why different variations on COF were recorded for each sample with sliding time.[49] Moreover, the reinforcement nanoparticles in the composites supported the applied load which helped to reduce the contact point between the ball and the counter bodies, resulting in lowering the average COF and mitigated excessive scratch and cut from the materials' surfaces.

Figure 10 shows the comparison of the specific wear rates between Ti6Al4V alloy matrix and the
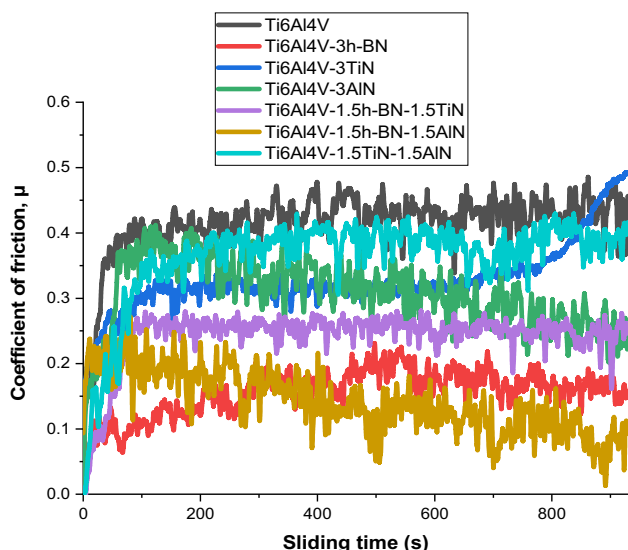
Fig. 8. Representative variations of the COF of the sintered samples (under an applied load of 10 N).
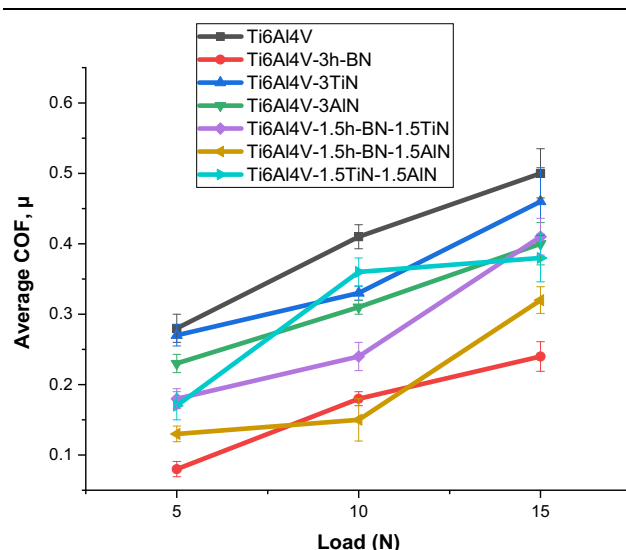
Fig. 9. Comparison of the average COF of the sintered samples under applied loads of 5 N, 10 N and 15 N.

TMC samples under the applied normal loads of 5 N, 10 N and 15 N. As expected, the specific wear rates of the unreinforced Ti6Al4V alloy sample at each applied load of 5 N ($3.391 \pm 0.141 \times 10^{-4}$ mm^3/Nm), 10 N ($7.272 \pm 0.32 \times 10^{-4}$ mm^3/Nm) and 15 N ($8.25 \pm 0.304 \times 10^{-4}$ mm^3/Nm) were higher than those of the TMCs attributed to the relatively low nanoindentation hardness value measured for the alloy as shown in Fig. 7c, because less hard materials typically demonstrate more wear than their counterparts under the same frictional conditions.[50,51] The specific wear rates of the materials increased linearly (see Fig. 10) as the load increased generally but much more markedly with the applied normal loads of 10 N and 15 N than 5 N for all reinforcement types (both single and double categories). The results suggested that the Ti6Al4V alloy matrix in the contact region underwent severe plastic deformation under the co-influence of the compression and shear stresses which produced the relatively large amount of wear obtained since the surface of worn materials have the inclination to be rough which predisposes the protective surface layers to impairment. Meanwhile, the incorporation of the harder reinforcement nanoparticles in the unreinforced Ti6Al4V alloy matrix reduced its ductility in the contact region, therefore bringing about much reduced wear.[49] In addition, according to the recognized linear Archard's wear law, the specific wear rate obtained is inversely proportional to the nanoindentation hardness and directly proportional to the applied normal loads:[46]

$$Q = \frac{KW}{H} \qquad (10)$$

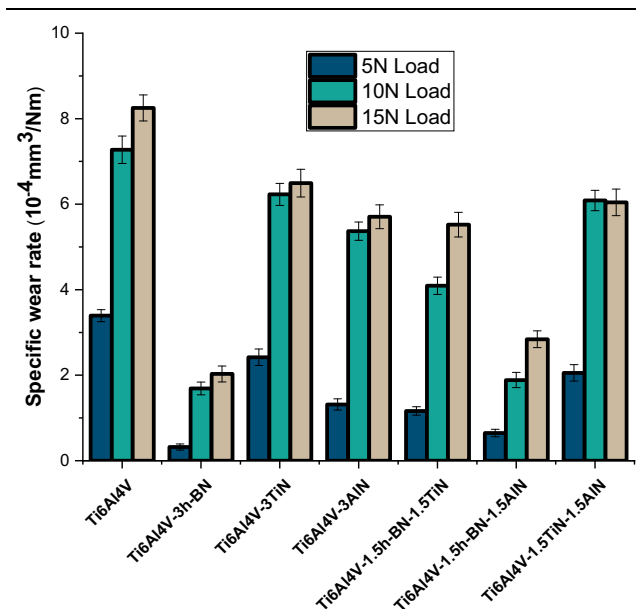In Eq. 10 above, Q stands for the volume of the worn material per unit sliding distance, W for the applied load, H for the worn material's hardness and K for the coefficient of wear. From the wear results obtained (as seen in Fig. 10), there is an indication that specific wear rates tended to vary in line with the Archard's wear equation.

The wear mechanisms and morphologies of the wear debris of the sintered samples at the end of the wear experiment were further examined by SEM as shown in Fig. 11(a–g). The wear mechanism as seen on the unreinforced matrix alloy (see Fig. 11a) originated from abrasive wear mainly generated by plastic deformation and micro-cutting of the ductile Ti6Al4V alloy matrix due to the steel ball rubbing action on the surface.[52,53] Further rubbing in the absence of lubrication led to an increase in the frictional force existing between the surfaces in the contact region bringing about severe surface failure attributed to inadequate resistance to adhesive wear. Following this, high temperature was generated, and loose wear debris was formed which continued to incite wear. With more sliding, the temperature increased and caused the wear debris to be work hardened and welded to the wear track surface of the matrix alloy.[54] As shown in Fig. 11c, d, e and g, the wear mechanisms of the TMCs and the morphologies of the accumulated wear debris observed are comparable to that of the unreinforced matrix alloy and indicated that the wear mechanisms are generally dominated by abrasive and adhesive wear. On the other hand, Fig. 11b and f showed more visible wear tracks on the TMCs with less residual welded debris unlike the unreinforced matrix and other TMCs with more debris volume accumulated along the wear tracks. It seems the reinforcement types play a significant role in determining the amount of wear debris. This is attributable to the substantial improvement in the wear resistance of the later TMCs through the single (3 wt.% of h-BN) and double (1.5 wt.% each of h-BN and AlN) reinforcements due to the influence of the self-lubricating feature of the h-BN particles and enhanced hardness profiles exhibited (see Fig. 7 c).

The wear mechanisms and the morphologies of the wear debris of the sintered samples at the end of the wear experiment were further examined by SEM as shown in Fig. 11(a–g). The wear mechanism as seen on the unreinforced matrix alloy (see Fig. 11a) originated from abrasive wear mainly generated by plastic deformation and micro-cutting of the ductile Ti6Al4V alloy matrix due to the steel ball rubbing action on the surface.[52,53] Further rubbing in the absence of lubrication led to an increase in the frictional force existing between the surfaces in the contact region bringing about severe surface failure attributed to inadequate resistance to adhesive wear. Following this, high temperature was generated, and loose wear debris was formed which continued to incite wear. With more sliding, the temperature increased and caused the wear debris to be work hardened and welded to the wear

Fig. 10. Comparison of the specific wear rates of the sintered samples under applied loads of 5 N, 10 N and 15 N.
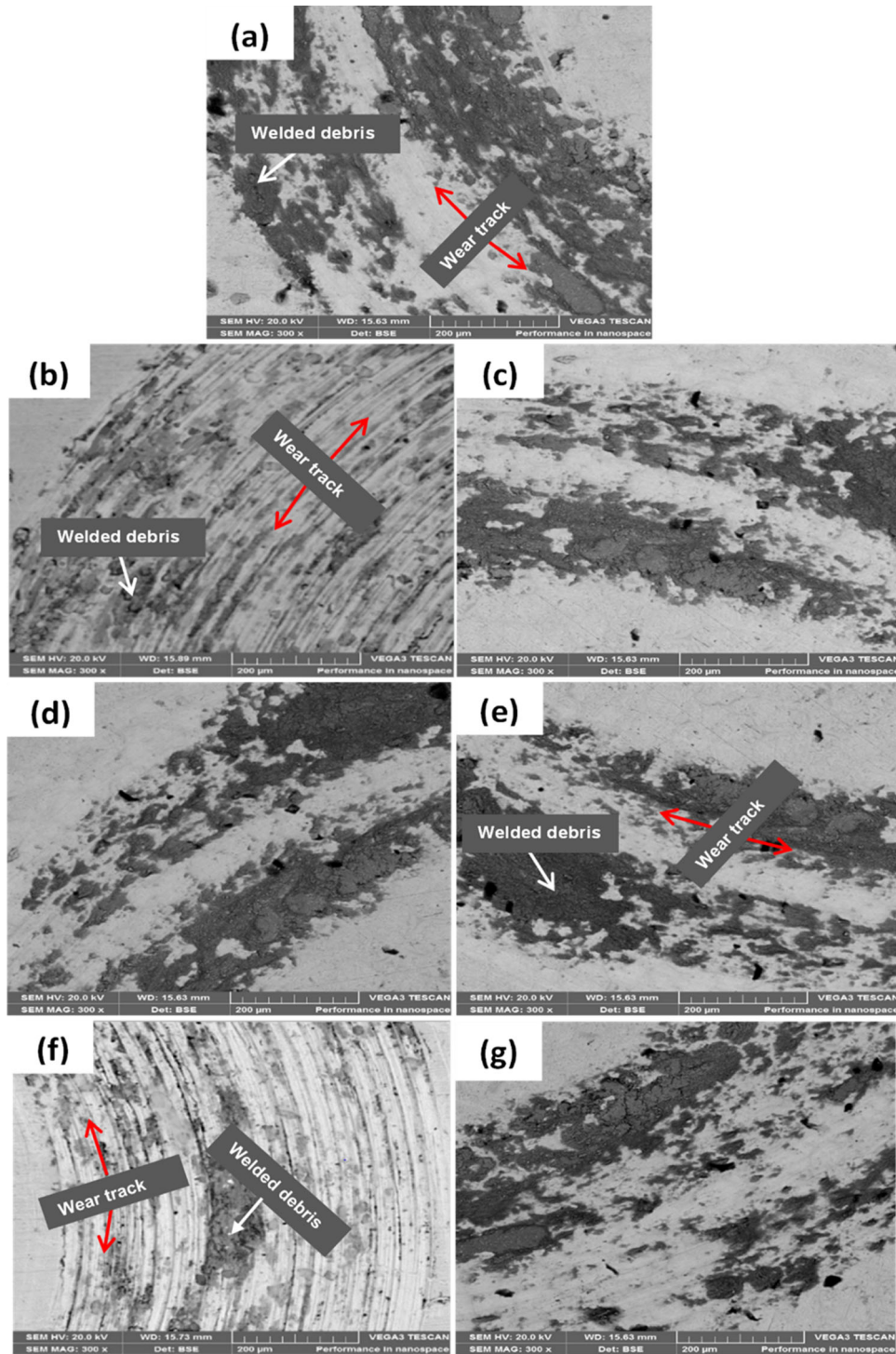
Fig. 11. Representative SEM micrographs of the worn surfaces of the sintered samples (under an applied load of 10 N).

track surface of the matrix alloy.[54] As shown in Fig. 11c, d, e and g, the wear mechanisms of the TMCs and the morphologies of the accumulated wear debris observed are comparable to those of the unreinforced matrix alloy and indicated that the wear mechanisms are generally dominated by abrasive and adhesive wear. On the other hand, Fig. 11b and f shows more visible wear tracks on the TMCs

with less residual welded debris unlike the unreinforced matrix and other TMCs with more debris volume accumulated along the wear tracks. It seems the reinforcement types play a significant role in determining the amount of wear debris. This is attributable to the substantial improvement in the wear resistance of the later TMCs through the single (3 wt.% of h-BN) and double (1.5 wt.% each of

h-BN and AlN) reinforcements due to the influence of the self-lubricating feature of the *h*-BN particles and enhanced hardness profiles exhibited (see Fig. 7 c).

CONCLUSION

In this work, particulate-reinforced TMCs made up of Ti6Al4V alloy matrix combined with single and double reinforcements, consisting of *h*-BN, TiN and AlN nanoparticles, respectively, have been developed via SPS technique. The effect of each reinforcement type on the ensuing properties was studied based on the microstructure, phase constituents, nanomechanical and tribological performance of the sintered TMCs, and conclusions are inferred as follows:

1. The SEM results showed that sintered TMCs consist of crack-free microstructures with practically no notable visible porosities or other major defects that may be detrimental to their ensuing properties. XRD results also indicated that impairing intermetallic phases were not detected suggesting that no adverse reactions occurred at the particle–matrix interfaces throughout the sintering operation. Meanwhile, the nano-reinforcements promoted grain refinement and broadening of the XRD peaks of the sintered TMCs, facilitated by smaller crystallite size and induced lattice strain. Thus, Ti6Al4V alloy and TMCs with single reinforcements (3 wt.% each) and different intermixed (1.5 wt.% each) reinforcements of *h*-BN, TiN and AlN nanoparticles, respectively, with desirable microstructures could be effectively synthesized by SPS technique.
2. The nanomechanical test results revealed remarkable improvements on the TMCs through each reinforcement type and can be arranged in decreasing order of influence from 3 wt.% *h*-BN, to 1.5 wt.% of *h*-BN and AlN, followed by 1.5 wt.% of *h*-BN and TiN, to 1.5 wt.% of TiN and AlN, then 3 wt.% AlN, and finally, 3 wt.% TiN. The observed outcome was found to be mainly due to the development of good particle–matrix bonding and mechanism of load transfer from the alloy matrix to the harder reinforcement particles of the sintered TMCs.
3. The COF values and specific wear rates of the sintered samples mostly increased with increasing applied normal loads and the TMCs showed general improvement in tribological properties as the nanoindentation hardness values increased by the incorporation of different reinforcement types.

ACKNOWLEDGEMENTS

CONFLICT OF INTEREST

On behalf of all authors, the corresponding author states that there is no conflict of interest.

REFERENCES

1. S. Diouf and A. Molinari, *Powd. Technol.* 221, 220 (2012).
2. P. Cavaliere, B. Sadeghi, and A. Shabani, Spark plasma sintering: process fundamentals, in *Spark Plasma Sintering of Materials*. ed. by P. Cavaliere (Springer, Cham, 2019).
3. W.R. Matizamhuka, *J. Southern Afr. Inst. Mining Metall.* 116(12), 1171 (2016).
4. F.M. Kgoete, A.P.I. Popoola, and O.S.I. Fayomi, *J. Alloys Compd.* 772, 943 (2019).
5. N.S. Weston, F. Derguti, A. Tudball, and M. Jackson, *J. Mater. Sci.* 50(14), 4860 (2015).
6. J.O. Abe, A.P.I. Popoola, O.M. Popoola, and E. Ajenifuja, Effects of refractory nitride reinforcements on the microstructure, densification and microhardness of Ti6Al4V-based binary composites produced by spark plasma sintering. In: Proceedings of IOP Conference Series: *Mater. Sci. Eng.*, Beijing, China, (2020), 784, 1, 012001.
7. H.O. Pierson, *Handbook of Refractory Carbides and Nitrides: Properties, Characteristics, Processing and Applications* (William Andrew, Norvich, 1996).
8. R.A. Khatavkar, A.K. Mandave, D.D. Baviskar, and S.L. Shinde, *Int. Res. J. Eng. Tech* 5, 3792 (2018).
9. L. Mahesh, J.S. Reddy, L.R. Jagadeesh, and M. Vinyas, The study of microstructure and wear behaviour of titanium nitride reinforced aluminium composites. In: Proceedings of AIP Conference Proceedings, (2020), 2204(1), 040014.
10. J.D. Avila and A. Bandyopadhyay, *J. Mat. Res.* 34(7), 1279 (2019).
11. E.R. de Araujo, M.M.S. de Souza, C.H. Gonzalez, and O.O. de Araújo Filho, *Mater. Sci. For.* 727, 259 (2012).
12. J.O. Abe, A.P.I. Popoola, and O.M. Popoola, *Mater. Sci. Eng. A* 774, 138920 (2020).
13. Y. Wen, L. Xie, Z. Wang, L. Wang, W. Lu, and L.C. Zhang, *J. Mat. Res. Technol.* 8(4), 3434 (2019).
14. J.O. Abe, O.M. Popoola, A.P.I. Popoola, E. Ajenifuja, and D.I. Adebiyi, *Eng. Res. Exp.* 1(2), 025043 (2019).
15. D.I. Adebiyi and A.P. Popoola, *Mater. Des.* 74, 67 (2015).
16. I.Y. Kim, B.J. Choi, Y.J. Kim, and Y.Z. Lee, *Wear* 271(9–10), 1962 (2011).
17. J.O. Abe, A.P.I. Popoola, and O.M. Popoola, Influence of varied process parameters on the microstructure, densification and microhardness of spark plasma sintered Ti-6Al-4V/h-BN binary composite. In: Proceedings of IOP Conference Series: *Mater. Sci. Eng.* (2019) 689, 1, 012005.
18. O.E. Falodun, B.A. Obadele, S.R. Oke, O.O. Ige, P.A. Olubambi, M.L. Lethabane, and S.W. Bhero, *Trans. Nonfer. Met. Soc. China* 28(1), 47 (2018).
19. O.E. Falodun, S.R. Oke, B.A. Obadele, A.M. Okoro, and P.A. Olubambi, *Met. Mater. Int.* 27, 1769 (2019).
20. R.R. Boyer, *Mater. Sci. Eng. A* 213(1–2), 103 (1996).
21. C. Leyens and M. Peters (eds.), *Titanium and Titanium Alloys: Fundamentals and Applications* (Wiley, Heidelberg, 2003).
22. M. Ji, L. Huang, Q. An, Y. Bao, X. Cui, Y. Jiao, and L. Geng, *Mater. Sci. Eng. A* 804, 140755 (2021).
23. G.M. Pharr and A. Bolshakov, *J. Mater. Res.* 17(10), 2660 (2002).
24. N.X. Randall, M. Vandamme, and F. Ulm, *J. Mater. Res.* 24(3), 679 (2009).

Assessment of Nanomechanical and Tribological Performance of Refractory Nitride-Reinforced
Titanium Alloy Matrix Composites Developed by Spark Plasma Sintering

805

25. K.K. Alaneme, O.P. Adu, S.R. Oke, O.E. Falodun, and P.A. Olubambi, *J. King Saud Uni-Eng. Sci.* 34(4), 282 (2020).
26. M.E. Maja, O.E. Falodun, B.A. Obadele, S.R. Oke, and P.A. Olubambi, *Ceram. Int.* 44, 4419 (2018).
27. C.O. Ujah, A.P.I. Popoola, O.M. Popoola, and V.S. Aigbodion, *Int. J. Adv. Manuf. Technol.* 100(5), 1563 (2019).
28. P.C. Dey, S. Sarkar, and R. Das, *Mater. Sci. Pol.* 38(2), 271 (2020).
29. M.S. Saravanan, K. Sivaprasad, P. Susila, and S.K. Babu, *Physica B* 406(2), 165 (2011).
30. W.C. Oliver and G.M. Pharr, *J. Mater. Res.* 7(6), 1564 (1992).
31. J.O. Abe, A.P.I. Popoola, O.M. Popoola, and E. Ajenifuja, *Int. J. Adv. Manuf. Technol.* 107(7), 2985 (2020).
32. H. Choe, S. Abkowitz, and S.M. Abkowitz, *Mater. Trans.* 49(9), 2153 (2008).
33. A.L. Rominiyi, M.B. Shongwe, L.C. Tshabalala, E.N. Ogunmuyiwa, S.O. Jeje, B.J. Babalola, and P.A. Olubambi, *J. Alloys Compd.* 848, 156559 (2020).
34. J. Sieniawski, R. Filip, and W. Ziaja, *Mater. Des.* 18(4–6), 361 (1997).
35. V. Nandal, R. Sarvesha, S.S. Singh, E.W. Huang, Y.J. Chang, A.C. Yeh, S. Neelakantan, and J. Jain, *J. Alloys Compd.* 855, 157521 (2021).
36. B. Sahoo, J. Joseph, A. Sharma, and J. Paul, *J. Compos. Mater.* 53(2), 261 (2019).
37. S.K. Mishra, H. Roy, A.K. Lohar, S.K. Samanta, S. Tiwari, and K. Dutta, A comparative assessment of crystallite size and lattice strain in differently cast A356 aluminium alloy. In: IOP Conference Series: Materials Science and Engineering (Vol. 75, No. 1, 012001). IOP Publishing. (2015).
38. A.D. Prasetya, M. Rifai, and H. Miyamoto, X-ray diffraction (XRD) profile analysis of pure ECAP-annealing Nickel samples. In: Journal of Physics: Conference Series (Vol. 1436, No. 1, 012113). IOP Publishing. (2020).
39. R. Filip, K. Kubiak, W. Ziaja, and J. Sieniawski, *J. Mater. Process. Technol.* 133(1–2), 84 (2003).
40. A.M. Okoro, R. Machaka, S.S. Lephuthing, S.R. Oke, M.A. Awotunde, and P.A. Olubambi, *Mater. Sci. Eng. A* 765, 138320 (2019).
41. S. Madeira, A.M.P. Pinto, L.C. Rodrigues, O. Carvalho, G. Miranda, R.L. Reis, J. Caramês, and F.S. Silva, *Mater. Des.* 120, 394 (2017).
42. D. Lin, M. Saei, S. Suslov, S. Jin, and G.J. Cheng, *Sci. Rep.* 5(1), 1 (2015).
43. P. Zhang, S.X. Li, and Z.F. Zhang, *Mater. Sci. Eng. A* 529, 62 (2011).
44. S. Ehtemam-Haghighi, G. Cao, and L. Zhang, *J. Alloys Compd.* 692, 892 (2017).
45. P. Madhukar, N. Selvaraj, C.S.P. Rao, and G.V. Kumar, *J. Alloys Compd.* 815, 152464 (2020).
46. A. Alizadeh and E. Taheri-Nassaj, *Mater. Charact.* 67, 119 (2012).
47. B.J. Choi, I.Y. Kim, Y.Z. Lee, and Y.J. Kim, *Wear* 318(1–2), 68 (2014).
48. J.L. Li and D.S. Xiong, *Wear* 265(3–4), 533 (2008).
49. M.K. Akbari, S. Rajabi, K. Shirvanimoghaddam, and H.R. Baharvandi, *J. Compos. Mater.* 49, 3665 (2015).
50. P.K. Rohatgi, M. Tabandeh-Khorshid, E. Omrani, M.R. Lovell, and P.L. Menezes, Tribology of metal matrix composites, in *Tribology for Scientists and Engineers*. ed. by P. Menezes, M. Nosonovsky, S. Ingole, S. Kailas, and M. Lovell (Springer, New York, 2013).
51. K.H. Zum Gahr, M. Mathieu, and B. Brylka, *Wear* 263(7–12), 920 (2007).
52. K. Kato, *Wear* 241, 151 (2000).
53. F. Eskandari, M. Atapour, M.A. Golozar, B. Sadeghi, and P. Cavaliere, *Tri. Mat. Sur. Iner.* 13(3), 172 (2019).
54. R.M. Mahamood, E.T. Akinlabi, M. Shukla, and S. Pityana, *Mater. Des.* 50, 656 (2013).